


Piezoelectric wind energy harvester for low-power sensors

Jayant Sirohi and Rohan Mahadik

Journal of Intelligent Material Systems and Structures
22(18) 2215–2228
© The Author(s) 2011
Reprints and permissions:
sagepub.co.uk/journalsPermissions.nav
DOI: 10.1177/1045389X11428366
jim.sagepub.com


Abstract

There has been increasing interest in wireless sensor networks for a variety of outdoor applications including structural health monitoring and environmental monitoring. Replacement of batteries that power the nodes in these networks is maintenance intensive. A wind energy-harvesting device is proposed as an alternate power source for these wireless sensor nodes. The device is based on the galloping of a bar with triangular cross section attached to a cantilever beam. Piezoelectric sheets bonded to the beam convert the mechanical energy into electrical energy. A prototype device of size approximately 160×250 mm was fabricated and tested over a range of operating conditions in a wind tunnel, and the power dissipated across a load resistance was measured. A maximum power output of 53 mW was measured at a wind velocity of 11.6 mph. An analytical model incorporating the coupled electromechanical behavior of the piezoelectric sheets and quasi-steady aerodynamics was developed. The model showed good correlation with measurements, and it was concluded that a refined aerodynamic model may need to include apparent mass effects for more accurate predictions. The galloping piezoelectric energy-harvesting device has been shown to be a viable option for powering wireless sensor nodes in outdoor applications.

Keywords

wind energy, energy harvesting, piezoelectric, galloping

Introduction

The availability of low-power microprocessors and sensors, in conjunction with data loggers and wireless communication, is enabling a wide range of distributed sensing applications. An example of such an application is a network of sensor nodes distributed over a large civil structure, such as a bridge (Kim et al., 2007; Wang et al., 2006), where each node senses local parameters such as vibration amplitude or strain. These data can be transmitted wirelessly to a base station or stored locally for future interrogation. In this way, the state or health of the structure can be monitored. Wireless sensor networks are also used in a number of environmental monitoring applications (Badrinath et al., 2000; Estrin et al., 2000; Evans and Bergman, 2007; Wang et al., 2006).

Yick et al. (2008) discussed several commercially available wireless sensors, their vendors, and their applications. The energy requirement of each node is typically small and can be met by a battery pack. For example, Mainwaring et al. (2002) described a sensor network in an ecological reserve to monitor seabird nesting, in which each sensor node required 6.9 mAh per day.

Replacement of depleted batteries for large sensor networks can be expensive, time consuming, and environmentally unfriendly. To overcome these issues, there has been increasing interest in the use of energy-harvesting methods to power the sensors on-site. This approach eliminates the need for batteries, and the associated requirement of periodic replacement and disposal. This is especially important in outdoor locations with inaccessible terrain, or geological parks where human interaction is minimum and environmental impact is key. There have been numerous studies on harvesting the energy in ambient structural vibrations using piezoelectric materials. Because a majority of wireless sensors are located outdoors, powering them by means of wind could also be a practical alternative. Aeroelastic instabilities such as flutter and galloping have been explored for harvesting energy from wind.

Department of Aerospace Engineering and Engineering Mechanics, The University of Texas at Austin, Austin, TX, USA

Corresponding author:

Jayant Sirohi, Department of Aerospace Engineering and Engineering Mechanics, The University of Texas at Austin, Austin, TX 78712, USA
Email: jayant.sirohi@mail.utexas.edu

Energy Harvesting Using Piezoelectric Materials

The electromechanical coupling exhibited by piezoelectric materials can be harnessed to extract electrical energy from mechanical vibrations. As a result, piezoelectric materials have found wide application as low-power generators. In a majority of these applications, the piezoelectric material extracts energy from ambient structural vibrations by operating as a base-excited oscillator. Sodano et al. (2004) provided an overview of several studies related to piezoelectric energy harvesting, including devices based on impact; wearable energy-harvesting devices based on motion of the human body; and devices designed to power wireless sensors. They also discussed methods to accumulate the harvested energy, using rechargeable batteries, capacitors, or flyback converters. While most of the energy-harvesting devices are based on cantilever beams, other geometries such as annular piezoelectric unimorphs/bimorphs have also been explored (Kauffman and Lesieutre, 2009).

duToit et al. (2005) investigated vibration-based piezoelectric energy harvesters to power MEMS-scale autonomous sensors. They compared the power density of electrostatic, electromechanical, and piezoelectric vibration-based energy harvesters and concluded that the piezoelectric devices have the highest power density based on volume.

Vibration-based piezoelectric energy harvesters are limited to relatively low-power outputs, on the order of 1–1000 μW (see duToit et al., 2005) due to the inherently low levels of strain energy in structural vibrations. Therefore, optimizing the power conditioning and storage electronics is an important part of the overall device (see Ottman et al., 2003).

It is interesting to note that vibrational energy harvesting using piezoelectric materials is closely related to piezoelectric shunt damping because both concepts extract energy from the structure, resulting in an effective negative damping. However, in the case of energy harvesting, the goal is to accumulate the energy while in the case of shunt damping, the goal is to dissipate as much of the energy as possible.

Energy Harvesting from Aeroelastic Instabilities

Some piezoelectric energy-harvesting devices have been developed to harness energy from structural vibrations induced by wind (Tan and Panda, 2007; Wang and Ko, 2010). Robbins et al. (2006) investigated the use of flexible, flag-like, piezoelectric sheets to generate power while flapping in an incident wind. The energy that can be harvested using these approaches is comparable to that of a vibration-based device. By exploiting structures with aeroelastic instabilities, it is possible to extract significantly higher amounts of energy from the wind. Bryant and Garcia (2011) developed a device to

harvest energy from flutter, using a piezoelectric bimorph with a flap at its tip. Linear and nonlinear models were developed to predict the performance of the device. The device generated an output power on the order of 2 mW.

Galloping is an aeroelastic instability involving low-frequency, large-amplitude oscillations of the structure normal to the direction of incident wind. Typically, it occurs in lightly damped structures with asymmetric cross sections, such as ice-covered transmission lines. There have been several studies on the effect of various parameters influencing galloping behavior of prismatic structures with different cross sections (Blevins, 2001), such as rectangular (Kazakevich and Vasilenko, 1996), D-section (Laneville et al., 1977; Ratkowski, 1961), triangular (Alonso et al., 2005, 2007; Alonso and Meseguer, 2006), and elliptic (Alonso et al., 2010). Barrero-Gil et al. (2010) theoretically investigated the feasibility of energy harvesting from structures undergoing galloping. They represented the sectional aerodynamic characteristics using a cubic polynomial and obtained an expression for the harnessable energy. Specific methods for energy extraction were not discussed. Nondimensional parameters defining the achievable power density and efficiency of energy conversion were derived. Sirohi and Mahadik (2011) investigated wind energy harvesting using a beam with piezoelectric sheets attached to a galloping tip body with D-shaped cross section. The variation of the power generated by the piezoelectrics was measured as a function of wind speed. The device produced a maximum power on the order of 0.5 mW.

This article describes a wind energy-harvesting device based on a galloping triangular section attached to cantilever beams with surface-bonded piezoelectric sheets. A prototype is tested and the results correlated with an analytical model. Such a device has the primary advantages of simplicity and robustness and could be collocated with the outdoor wireless sensors to power them using renewable wind energy.

Galloping Piezoelectric Energy Harvester

The galloping piezoelectric energy-harvesting device investigated in this article consists of a prismatic rigid body attached to the tip of two aluminum cantilever beams that act like a flexible support. Piezoelectric sheets are bonded near the root of the beams, at the location of maximum strain energy. Galloping of the prismatic body in an incident wind results in large-amplitude oscillatory bending of the beams that is converted into electrical energy by the piezoelectric sheets. While the tip body can have any cross section that is prone to galloping, the device described in this article has a tip body with an equilateral triangle cross section (Figure 1). Wind incident on the flat face of the

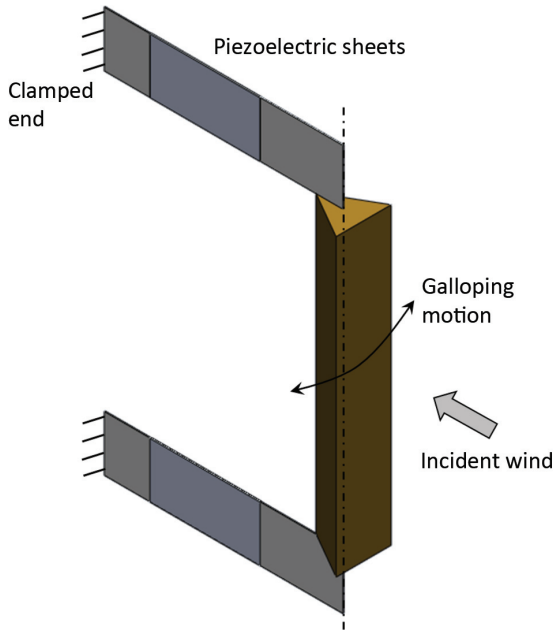


Figure 1. Galloping energy harvester with tip body having equilateral triangle cross section.

triangular section results in galloping motion and bending of the cantilever beams.

Physical Principles

Den Hartog (1956) explained the phenomenon of galloping for the first time in 1934 and introduced a criterion for galloping stability of a structure. He developed a criterion for galloping to occur on a section having specified lift and drag coefficients, on a flexible support with mechanical damping. The Den Hartog stability criterion states that a section on a flexible support with negligible mechanical damping is susceptible to galloping when

$$H(\alpha) = \left(\frac{dC_l}{d\alpha} + C_d \right) > 0 \quad (1)$$

where C_l and C_d are the sectional lift and drag coefficients, respectively, and α is the sectional angle of attack. The quantity $H(\alpha)$ is referred to as the Den Hartog factor. Note that galloping occurs at high angles of attack where the aerodynamic coefficients are highly nonlinear. Therefore, the criterion is evaluated by considering a linearized slope of C_l versus α at the equilibrium point about which oscillations occur. The onset of galloping is characterized by a negative effective damping of the system and corresponding exponential increase in the amplitude of motion with time. However, the system reaches a limit cycle oscillation in a short period of time, after which the amplitude of

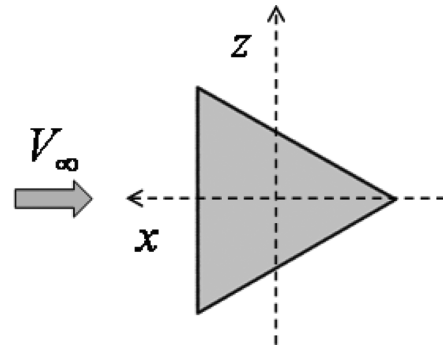


Figure 2. Incident velocity and coordinate system of section.

oscillation remains constant. Because the frequency of oscillation is relatively low, it has been observed that quasi-static aerodynamics are sufficient to model the behavior (Alonso et al., 2007; Barrero-Gil et al., 2010).

Consider a coordinate system with the x -axis along the span of the beam, y -axis along the beam width, and z -axis along the beam thickness. The bending displacement of the beam is given by $w(x)$. The sectional angle of attack of the tip body is then given by

$$\alpha = \alpha_0 - \tan^{-1} \left(\frac{\dot{w}_{tip}}{V_\infty} \right) \quad (2)$$

where α_0 is the initial angle of attack (when the section is at rest) with respect to the axes along which the sectional aerodynamic coefficients were measured, V_∞ is the magnitude of the incident wind (Figure 2), and \dot{w}_{tip} is the velocity of the beam tip.

At the steady-state condition, the extracted energy is equal to the work done on the system by the incident wind. Barrero-Gil et al. (2010) calculated a theoretical value of around 7% for the efficiency of converting wind energy into mechanical energy by galloping. Although this is low compared to the Betz limit for wind turbines, galloping energy harvesters can be an alternative in cases where robust, low-maintenance, low-power energy generation devices are required. The range of angles of attack over which galloping occurs indicates that the device is self-limiting in terms of amplitude as well as wind speed. Theoretically, the maximum amplitude of oscillation corresponds to a sectional angle of attack at which the Den Hartog criterion is no longer satisfied. Therefore, no additional precautions need be taken to protect the device in case of excessive wind speed.

Parameters of the Prototype Device

A prototype device was constructed for measurement of the power output and correlation with analysis. In addition to the beam geometry, the sectional

Table 1. Parameters of the prototype galloping wind energy harvester.

Parameter	Measurement (mm)
Beam length	161
Beam width	38
Beam thickness	0.635
Tip body length	251
Tip body dimension	40 (side)
Piezo sheet length	72.4
Piezo sheet width	36.2
Piezo sheet thickness	0.267

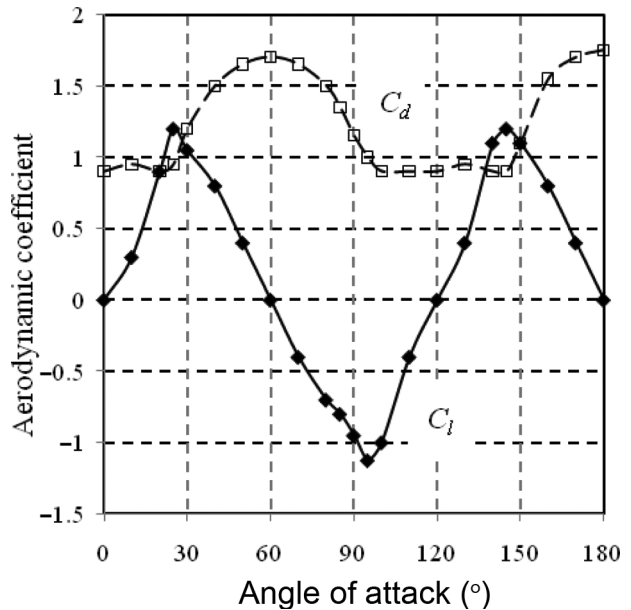
aerodynamic coefficients of the tip body are key to the performance of the device. Two identical aluminum beams were clamped to a support at one end and to a prismatic tip body at their other end. Two piezoelectric sheets (PSI-5H4E from Piezo Systems, Inc.) of length 72.4 mm, width 36.2 mm, and thickness 0.267 mm were bonded to the top and bottom surfaces of each beam with a high shear strength epoxy adhesive. After curing, the bond layer was measured to be approximately 0.025 mm thick. The piezoelectric sheets were connected in parallel with opposite polarity, because the top layer undergoes tension when the bottom layer is undergoing compression. In this way, the charges developed by the piezoelectric sheets are added together, and the effective capacitance is the sum of the capacitances of the individual sheets. The properties of the beam, tip body, and piezoelectric sheets are listed in Table 1.

An equilateral triangle section was chosen for the galloping device because it exhibits a favorable combination of a large range of operating angles of attack as well as high Den Hartog factor (see Alonso and Meseguer, 2006).

The sectional aerodynamic coefficients of an equilateral triangle section were measured by Alonso and Meseguer (2006) and are shown in Figure 3. The angle of attack for these data is with reference to a line of symmetry of the triangular section. From the figure, it is seen when the wind is incident normal to a face of the triangle (angle of attack of 60° with respect to a line of symmetry), the slope of C_l is negative, and C_d is relatively constant. In this condition, the Den Hartog condition is satisfied and the section is prone to galloping. It is also seen that the variation of aerodynamic coefficients with angle of attack is symmetric with respect to a line of symmetry of the triangle.

Analytical Model

Several analytical models have been proposed to quantify the electrical output from a piezoelectric energy harvester. Sodano et al. (2004) used Hamilton's principle to develop a coupled electromechanical model for a piezoelectric bimorph energy-harvesting device. Umeda et al. (1996) proposed an electrical equivalent circuit to

**Figure 3.** Aerodynamic coefficients of an equilateral triangle section (Alonso and Meseguer, 2006).

model the electrical energy generated by a metal ball falling on a plate with a bonded piezoelectric sheet. Roundy et al. (2004) discussed the operation and analytical modeling of a base-excited energy harvester consisting of a piezoelectric bimorph with a lumped mass attached to its tip. Ajitsaria et al. (2007) developed three different mathematical models for the voltage generated by a bimorph piezoelectric cantilever beam. Erturk and Inman (2009) modeled their device by coupling an Euler–Bernoulli beam representation with the piezoelectric constitutive laws.

In this article, an analytical model of the galloping energy-harvesting device is developed using a variational approach, in conjunction with assumed displacements and quasi-steady aerodynamic forcing. The goal of the model is to predict the voltage generated by the piezoelectric sheets as a function of time, for a given incident wind speed, beam geometry, and load resistance. This study focuses on the conversion of wind energy into electrical energy and does not consider storage of the generated electrical energy. Accordingly, the electrical load on the system is represented by a load resistance connected across the electrodes of the piezoelectric sheets, which dissipates energy in the form of Ohmic heating and acts as an additional positive damping on the system. Therefore, the amplitude of oscillation of the beam increases till a steady-state limit cycle is reached, wherein the energy extracted from the incident wind is exactly equal to the energy dissipated across the load resistance and by any structural damping.

The analytical model consists of two parts: the structural model and the aerodynamic model. Energy-harvesting devices of similar geometry and having

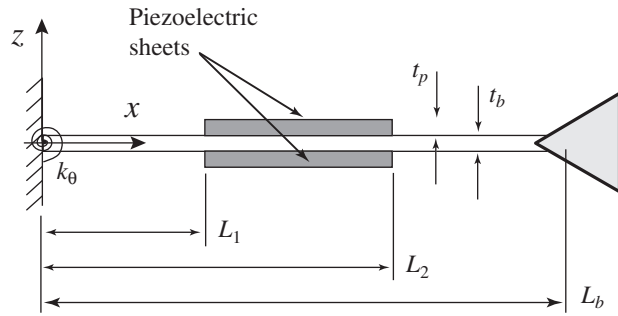


Figure 4. Schematic of beam with piezoelectric sheets and tip body.

different tip bodies can be modeled by simply changing the sectional aerodynamic coefficients.

Structural Model

A schematic of a single beam with the triangular tip body, indicating the coordinate directions and relevant dimensions, is shown in Figure 4. The device is modeled as two Euler–Bernoulli beams attached to a tip mass. To minimize blockage of the incident wind, the device must be clamped to a support with a low frontal area. Consequently, the support will have a lower stiffness than an ideal clamped boundary condition. The flexibility of the support is modeled by incorporating a torsional spring of stiffness k_θ (N/m) at the root of the beam.

The analytical model of the electromechanical coupling of the piezoelectric sheets is developed using an energy-based variational formulation. The basic procedure is to formulate a variational indicator incorporating the kinetic energy, potential energy, and nonconservative virtual work on the system. The potential energy includes contributions from the strain energy as well as stored electrical energy. Similarly, the nonconservative virtual work includes mechanical and electrical terms. The variational indicator can be set up in two ways based on the choice of independent variables, as described by Crandall et al. (1982).

In one approach, the variational indicator ($V.I.$) is written as

$$\begin{aligned} V.I. &= \int_{t_1}^{t_2} [\delta(T - V - W_e) + \sum_i f_i \delta w_i + \sum_j \nabla_j \delta q_j] dt \\ &= \int_{t_1}^{t_2} [\delta(T - U) + \sum_i f_i \delta w_i + \sum_j \nabla_j \delta q_j] dt \end{aligned} \quad (3)$$

where T is the kinetic energy of the structure, V is the strain energy, and W_e is the electrical energy. The summations represent the virtual work done by all nonconservative mechanical and electrical elements in the

system. In the present case, f_i are the transverse forces applied to the beam, w_i are the transverse displacements, ∇_j is the voltage drop across the nonconservative electrical elements (in this case, the load resistance), and q_j is the electric charge. The strain energy and electrical energy can be combined into an internal energy U given by

$$\begin{aligned} U(\boldsymbol{\varepsilon}, \mathbf{D}) &= V + W_e \\ &= \frac{1}{2} \int_{V_s} \boldsymbol{\sigma}^T \boldsymbol{\varepsilon} dV_s + \frac{1}{2} \int_{V_s} \mathbf{E}^T \mathbf{D} dV_s \end{aligned} \quad (4)$$

where $\boldsymbol{\varepsilon}$ is the strain vector, $\boldsymbol{\sigma}$ is the stress vector, \mathbf{D} is the electric displacement vector, \mathbf{E} is the electric field vector, and V_s is the volume of the structure. Note that the internal energy must be expressed as a function of independent variables corresponding to displacement and charge, which are in this case, $\boldsymbol{\varepsilon}$ and \mathbf{D} (see Mason, 1950). Several researchers have adapted this approach to model the electromechanical coupling in structures with piezoelectric material (duToit et al., 2005; Elvin et al., 2001; Hagood et al., 1990; Sodano et al., 2004).

Dietl and Garcia (2010) used an alternate approach, based on flux linkage, to optimize the shape of a piezoelectric beam for energy harvesting. In this approach, the variational indicator is written as

$$\begin{aligned} V.I. &= \int_{t_1}^{t_2} [\delta(T - V + W_e^*) + \sum_i f_i \delta w_i + \sum_j i_j \delta \lambda_j] dt \\ &= \int_{t_1}^{t_2} [\delta(T - H_2) + \sum_i f_i \delta w_i + \sum_j i_j \delta \lambda_j] dt \end{aligned} \quad (5)$$

where W_e^* is the electrical co-energy and i_j are the currents flowing through the dissipative electrical elements in the system. The λ_j are the flux linkages, which are related to voltages by

$$\nabla = \dot{\lambda} \quad (6)$$

The strain energy and electrical co-energy can be combined into an electrical enthalpy H_2 given by

$$\begin{aligned} H_2(\boldsymbol{\varepsilon}, \mathbf{E}) &= V - W_e^* \\ &= \frac{1}{2} \int_{V_s} \boldsymbol{\sigma}^T \boldsymbol{\varepsilon} dV_s - \frac{1}{2} \int_{V_s} \mathbf{D}^T \mathbf{E} dV_s \end{aligned} \quad (7)$$

Note that the electrical enthalpy must be expressed as a function of independent variables corresponding to displacement and electric field, which are in this case, $\boldsymbol{\varepsilon}$ and \mathbf{E} (see Mason, 1950). It can be shown that the approaches based on the two variational indicators are equivalent because the internal energy and electric enthalpy are related to each other by a Legendre transformation.

The formulation based on internal energy (Equation (3)) is used for the present analysis. The constitutive relations of the piezoelectric material are given as (IEEE, 1987)

$$\begin{Bmatrix} \boldsymbol{\varepsilon} \\ \mathbf{D} \end{Bmatrix} = \begin{bmatrix} \mathbf{s}^E & \mathbf{d}^T \\ \mathbf{d} & \mathbf{e}^\sigma \end{bmatrix} \begin{Bmatrix} \boldsymbol{\sigma} \\ \mathbf{E} \end{Bmatrix} \quad (8)$$

where \mathbf{d} is the matrix of piezoelectric coefficients, \mathbf{s} is the compliance matrix, and \mathbf{e} is the dielectric permittivity matrix. The superscripts E and σ refer to quantities measured at constant electric field and constant stress, respectively. The piezoelectric constitutive relations can be rearranged in terms of the strain and electric displacement as

$$\begin{Bmatrix} \boldsymbol{\sigma} \\ \mathbf{E} \end{Bmatrix} = \begin{bmatrix} \mathbf{c}^D & -\mathbf{h}^T \\ -\mathbf{h} & \boldsymbol{\beta}^e \end{bmatrix} \begin{Bmatrix} \boldsymbol{\varepsilon} \\ \mathbf{D} \end{Bmatrix} \quad (9)$$

In the case of the present device, the piezoelectric sheets are attached so that their 1-axis is along the length of the beam (x -direction) and the 3-axis is along the thickness of the beam (z -direction). Strains along the y -direction are ignored, and a one-dimensional representation is used to model the device. Reducing Equation (9) to one dimension and substituting the relevant piezoelectric constants from Equation (8) yield

$$\begin{Bmatrix} \sigma_{11} \\ E_3 \end{Bmatrix} = \begin{bmatrix} Y_{11}^D & -\frac{1}{d'_{31}} \\ -\frac{1}{d'_{31}} & \frac{1}{e_{33}^e} \end{bmatrix} \begin{Bmatrix} \varepsilon_{11} \\ D_3 \end{Bmatrix} \quad (10)$$

where

$$Y_{11}^D = \frac{Y_{11}^E}{1 - k_{31}^2} = \frac{1}{s_{11}^E (1 - k_{31}^2)} \quad (11)$$

$$d'_{31} = \frac{d_{31}(1 - k_{31}^2)}{k_{31}^2} \quad (12)$$

$$e_{33}^e = e^\sigma (1 - k_{31}^2) \quad (13)$$

The superscripts D and ε refer to quantities measured at constant electric displacement and constant strain, respectively. The quantity Y_{11} is the Young's modulus of the piezoelectric material. In these equations, the electromechanical coupling factor of the piezoelectric sheets is defined as

$$k_{31}^2 = \frac{d_{31}^2 Y_{11}^E}{e_{33}^\sigma} \quad (14)$$

It is convenient to model the coupled behavior of the piezoelectric sheets in this way because it is relatively simple to measure the constants Y_{11}^E , d_{31} , and e_{33}^σ . Substituting these quantities into Equation (5) yields the internal energy of the device as

$$\begin{aligned} U &= \frac{1}{2} \int_{V_s} \sigma_{11} \varepsilon_{11} \, dV_s + \frac{1}{2} \int_{V_s} D_3 E_3 \, dV_s \\ &= \frac{1}{2} \int_{V_s} \left(Y_{11}^D \varepsilon_{11}^2 + \frac{D_3^2}{e_{33}^e} \right) dV_s - \int_{V_s} \frac{D_3 \varepsilon_{11}}{d'_{31}} \, dV_s \end{aligned} \quad (15)$$

The integration is performed over the volume of the entire structure, taking care to set the appropriate material constants over the piezoelectric elements and the aluminum beam. Applying the Euler–Bernoulli assumption to the aluminum beams results in the longitudinal strain given by

$$\varepsilon_{11} = -zw'' \quad (16)$$

A superposition of assumed shape functions $\phi(x)$ and generalized displacement coordinates $r(t)$ is used to represent the transverse deflection as

$$w(x, t) = \sum_{i=1}^N \phi(x) r(t) = \boldsymbol{\phi} \mathbf{r} \quad (17)$$

which gives the longitudinal strain as

$$\varepsilon_{11} = -z\boldsymbol{\phi}' \mathbf{r} \quad (18)$$

Note that the potential energy stored in the torsional spring (of stiffness k_θ in Newton meters per radian) at the root of the beam, given by V_{spring} , must be added to the internal energy of the structure.

$$V_{spring} = \frac{1}{2} k_\theta [w'(0)]^2 \quad (19)$$

The angular deflection at the root of the beam is given by

$$w'(0) = \boldsymbol{\phi}'(0) \mathbf{r} \quad (20)$$

The electric displacement can be represented as a summation of assumed functions $\psi(z)$ and generalized charge coordinates $q(t)$ as

$$D(z, t) = \sum_{j=1}^M \psi_j(z) q(t) = \boldsymbol{\psi} \mathbf{q} \quad (21)$$

Note that if the electric field across the piezoelectric sheets is assumed to be a constant:

$$\psi = \frac{1}{A_p} \quad (22)$$

where A_p is the area of the electrodes on the piezoelectric sheets. In this case, the electric displacement is given by

$$D = \frac{q}{A_p} \quad (23)$$

where q is the physical charge generated by the piezoelectric sheets. The assumption of constant electric field across the piezoelectric sheets will be retained for the remainder of this analysis. Substituting the strain and electric displacement into Equation (15), and including the potential energy of the root spring, the internal energy can be written as

$$U = \frac{1}{2} \mathbf{r}^T \mathbf{K} \mathbf{r} + \frac{1}{2} \frac{q^2}{C_p} + \mathbf{r}^T \mathbf{\Theta} q \quad (24)$$

where the stiffness matrix \mathbf{K} and the coupling matrix $\mathbf{\Theta}$ are given by

$$\mathbf{K} = \int_{V_p} Y_{11}^D z^2 \boldsymbol{\phi}''^T \boldsymbol{\phi}'' dV_p + \int_{V_b} Y_b z^2 \boldsymbol{\phi}''^T \boldsymbol{\phi}'' dV_b + \boldsymbol{\phi}'(\mathbf{0})^T k_\theta \boldsymbol{\phi}'(\mathbf{0}) \quad (25)$$

$$\mathbf{\Theta} = \int_{V_p} \frac{z \boldsymbol{\phi}''^T}{d'_{31} A_p} dV_p \quad (26)$$

The subscripts b and p denote quantities corresponding to the beam and the piezoelectric sheets, respectively.

Note that the capacitance of the piezoelectric sheets (at constant strain) is given by

$$C_p = \frac{e_{33}^2 A_p}{t_p} \quad (27)$$

The kinetic energy of the structure is given by

$$T = \frac{1}{2} \int_{V_s} \rho \dot{w}^2 dV_s + \frac{1}{2} M_{tip} (\dot{w}(L_b))^2 = \frac{1}{2} \dot{\mathbf{r}}^T \mathbf{M} \dot{\mathbf{r}} \quad (28)$$

where the mass matrix is

$$\mathbf{M} = \int_{V_b} \rho_b \boldsymbol{\phi}^T \boldsymbol{\phi} dV_b + \int_{V_p} \rho_p \boldsymbol{\phi}^T \boldsymbol{\phi} dV_p + \boldsymbol{\phi}(L_b)^T M_{tip} \boldsymbol{\phi}(L_b) \quad (29)$$

In the case of the energy-harvesting device under consideration, the nonconservative mechanical virtual work arises only due to the aerodynamic force F_{tip} acting on the tip body. The nonconservative electrical virtual work is the energy dissipated by the load resistance R_L .

Substituting the internal energy (Equation (24)), kinetic energy ((Equation (28)), and nonconservative virtual works into Equation (3) and setting the variational indicator to zero,

$$\delta \int_{t_1}^{t_2} [\delta(T - U) + F_{tip} \delta w(L_b) + \mathbb{V} \delta q] dt = 0 \quad (30)$$

yields the equations of motion of energy-harvesting device as

$$\mathbf{M} \ddot{\mathbf{r}} + \mathbf{K} \mathbf{r} + \mathbf{\Theta} q = F_{tip} \boldsymbol{\phi}(L_b) \quad (31)$$

$$\mathbf{\Theta}^T \mathbf{r} + \frac{1}{C_p} q - \mathbb{V} = 0 \quad (32)$$

In the present case, the voltage drop across the load resistance is given by

$$\mathbb{V} = -R_L \dot{q} \quad (33)$$

The mechanical damping of the structure is incorporated into the model in terms of a proportional damping matrix (see Sodano et al., 2004) \mathbf{C} given by

$$\mathbf{C} = \alpha \mathbf{M} + \beta \mathbf{K} \quad (34)$$

where the constants α and β are determined from

$$\zeta_k = \frac{\alpha}{2\omega_k} + \frac{\beta\omega_i}{2} \quad (i = 1, 2 \dots N) \quad (35)$$

In the above equation, ω_k is the natural frequency of the k th mode, ζ_k is the modal damping, and N is the number of modes (equal to the dimension of the mass and stiffness matrices). These quantities are measured experimentally from the impulse response of the beam with an appropriate electrical boundary condition for the piezoelectric sheets. An additional damping is introduced due to the energy dissipation in the internal resistance of the piezoelectric sheets, R_i . This resistance is a function of the dissipation factor (expressed as $\tan \delta$) of the piezoelectric material. For small values of $\tan \delta$, the internal resistance can be written as (Sirohi and Chopra, 2000)

$$R_i = \frac{\tan \delta}{\omega C_p} \quad (36)$$

where ω is the frequency of voltage across the electrodes of the piezoelectric sheet. At large values of electric field, the dissipation factor and other piezoelectric constants become nonlinear functions of the electric field. However, this effect is neglected in the present analysis. The parameters of the piezoelectric sheets used in the analysis are listed in Table 2.

The equations of motion can be written in the state space form by defining a state vector containing the

Table 2. Parameters of piezoelectric material

Piezoelectric property	Symbol	Value
Strain coefficient (pC/N)	d_{31}	-320
Young's modulus (GPa)	Y_{11}^E	62
Dielectric constant (nF/m)	ϵ_{33}^T	33.65
Density (kg/m ³)	ρ_p	7800

generalized displacement (consisting of N assumed modes), generalized velocity, and charge:

$$\mathbf{x} = \begin{Bmatrix} \mathbf{r} \\ \dot{\mathbf{r}} \\ q \end{Bmatrix} \quad (37)$$

The equations of motion (Equations (32) and (33)) can then be written as

$$\dot{\mathbf{x}} = \begin{bmatrix} \mathbf{0}_{(N \times N)} & \mathbf{I}_{(N \times N)} & \mathbf{0}_{(N \times 1)} \\ -\mathbf{M}^{-1}\mathbf{K} & -\mathbf{M}^{-1}\mathbf{C} & -\mathbf{M}^{-1}\Theta \\ -\frac{1}{R_L}\Theta^T & \mathbf{0}_{(1 \times N)} & -\frac{1}{R_L C_p} \end{bmatrix} \mathbf{x} + \begin{Bmatrix} \mathbf{0}_{(N \times 1)} \\ \mathbf{M}^{-1}\Phi(\mathbf{L}_b)^T \\ 0 \end{Bmatrix} F_{tip} \quad (38)$$

The present analysis assumes a two-term approximation for the transverse deflection as

$$w(x, t) = \phi_1 r_1 + \phi_2 r_2 = \left(\frac{x}{L_b}\right) r_1 + \left(\frac{x}{L_b}\right)^3 r_2 \quad (39)$$

The first assumed mode represents the deformation of the support (root torsional spring), and the second mode represents the bending of the beam. The assumption of a single bending deflection shape is consistent with visual observations of the beam deformation during galloping. In addition, the system is expected to gallop at a frequency close to its first mode, and consequently, a shape function proportional to its static deflection is chosen to approximate this mode shape.

Substituting the assumed deflection and electric displacement into Equations (25), (26), and (30), we get expressions for the effective mass and stiffness matrices, and the electromechanical coupling matrix.

$$M_{11} = \frac{\rho_b b_b t_b L_b}{3} + \frac{2\rho_p b_p t_p (L_2^3 - L_1^3)}{3L_b^2} + M_{tip} \quad (40)$$

$$M_{12} = M_{21} = \frac{\rho_b b_b t_b L_b}{5} + \frac{2\rho_p b_p t_p (L_2^5 - L_1^5)}{5L_b^4} + M_{tip} \quad (41)$$

$$M_{22} = \frac{\rho_b b_b t_b L_b}{7} + \frac{2\rho_p b_p t_p (L_2^7 - L_1^7)}{7L_b^6} + M_{tip} \quad (42)$$

$$K_{11} = \frac{k_\theta}{L_b^2} \quad (43)$$

$$K_{12} = K_{21} = 0 \quad (44)$$

$$K_{22} = \frac{Y_b b_b t_b^3}{L_b^3} + \frac{8Y_{11}^D b_p (L_2^3 - L_1^3)}{L_b^6} \left[\left(\frac{t_b}{2} + t_p\right)^3 - \left(\frac{t_b}{2}\right)^3 \right] \quad (45)$$

$$\Theta_1 = 0 \quad (46)$$

$$\Theta_2 = \frac{3d_{31} Y_{11}^E b_p}{L_b^3 C_p t_p} t_p (t_b + t_p) (L_2^2 - L_1^2) \quad (47)$$

Aerodynamic Model

In the present galloping device, the force acting on the tip body is calculated assuming quasi-static, two-dimensional aerodynamics. The vertical sectional force per unit length (F_z) is multiplied by the length of the tip body (L_{tip}) to give the total tip force (F_{tip}). Components of the sectional lift L and sectional drag D per unit length contribute to the force F_z .

$$F_{tip} = F_z L_{tip} = (L \cos \alpha + D \sin \alpha) L_{tip} \quad (48)$$

The quasi-static angle of attack at each section of the tip body is given by

$$\alpha = \tan^{-1} \left(\frac{\dot{w}(L_b)}{V_\infty} \right) + w'(L_b) \quad (49)$$

where the first term is due to the relative wind velocity and the second term is due to the structural deformation. The sectional lift and drag per unit length are given by

$$L = \frac{1}{2} \rho (V_\infty^2 + \dot{w}^2(L_b)) b_{tip} C_l \quad (50)$$

$$D = \frac{1}{2} \rho (V_\infty^2 + \dot{w}^2(L_b)) b_{tip} C_d \quad (51)$$

where C_l and C_d are the sectional lift and drag coefficients, respectively; b_{tip} is the width of the tip body; and ρ is the density of air. The sectional aerodynamic coefficients depend on the quasi-static angle of attack as well as Reynolds number. The coefficients that were used in the analysis are plotted in Figure 3. Note that these data were measured at a different Reynolds number than the present experiment. This could be a source of discrepancy while correlating predictions based on these coefficients with measurements. Recall that the angle of attack for these data is indexed to a line of symmetry of the triangular section. Because the wind is incident on a face of the triangle in the present device, a constant offset of $\alpha_o = 60^\circ$ must be added to the angle of attack calculated from Equation (50) to obtain the angle of attack corresponding to Figure 3.

Solution Procedure

The governing equations of the system were solved by time marching using MATLAB. A small displacement of the beam ($r_1 = 0.001''$) was set as an initial condition. All initial velocities and initial charge were set to 0. This corresponded to an initial angle of attack of approximately 1° . It was found that small variations in the initial angle of attack in this range did not affect the solution.

At each time step, the angle of attack calculated from Equation (50) was used to perform a table lookup to find the aerodynamic coefficients. These were then used to find the sectional lift and drag, from which the

force on the tip body was calculated. The block diagram shown in Figure 5 summarizes the solution procedure. The model predicts beam displacement $w(x, t)$ and power generated for given values of incident wind velocity, load resistance, and device geometry. Tip bodies of any cross-sectional geometry can be evaluated by incorporating the appropriate sectional airfoil characteristics in the form of a table lookup.

Experimental Setup and Procedure

A prototype galloping device was constructed and tested to validate the analytical model. The parameters of the device are listed in Table 1. The tip body was constructed out of rigid foam and mounted on the beams such that its angle of incidence could be manually adjusted. The prototype was assembled in the test section of a closed-circuit, open-jet wind tunnel. The installation is shown in Figure 6, in which the triangular section is aligned such that it does not gallop.

The power generated by the galloping device was measured at several wind velocities. At a specific value

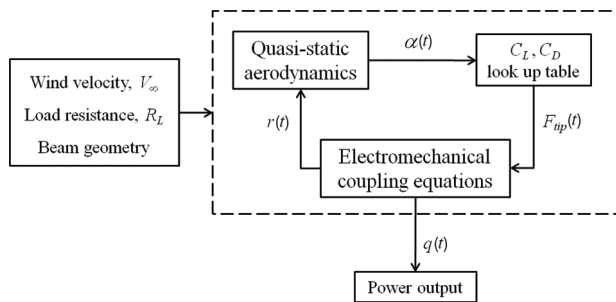


Figure 5. Block diagram of solution procedure.

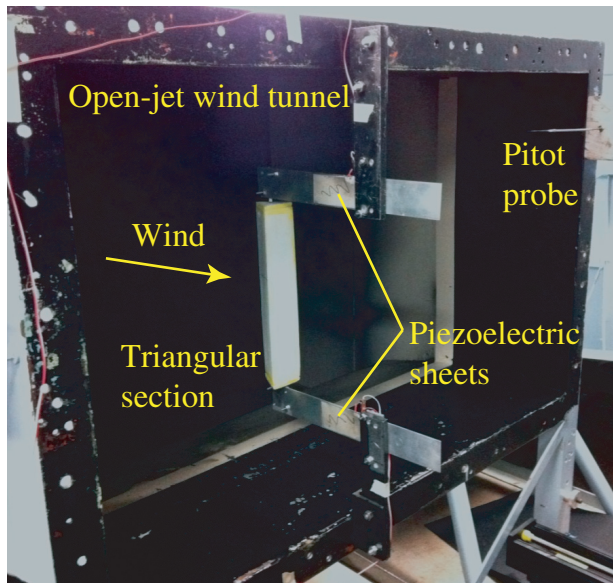


Figure 6. Prototype galloping device installed in the wind tunnel in test section.

of wind velocity, a load resistance was connected across the electrodes of the piezoelectric sheets. The tip body was manually rotated so that the wind was incident normal to a flat face, and then released. Small perturbations generated by vortex shedding and turbulence in the airstream caused the device to start galloping. The voltage developed across the load resistance as a function of time was measured. After the voltage reached a steady state, the galloping was manually arrested and the procedure repeated with a different load resistance. The power generated was calculated over a range of incident wind speeds by varying the load resistance across the piezoelectric sheets and measuring the voltage across them at each wind speed. A NI 9205 data acquisition system in conjunction with Labview was used to acquire the data. Because the generated voltage was, in most cases, greater than 10 V, a voltage divider circuit was used to scale it down to the range of the data acquisition system. The resistance of the voltage divider was chosen to be much higher than the output impedance of the piezoelectric sheets so that it did not contribute to the load resistance. In addition, the output of the voltage divider was buffered by a unity gain operational amplifier so that it would not be affected by the input impedance of the data acquisition system. The wind speed was measured by a conventional pitot probe and manometer.

Results and Discussion

Prior to measuring the power output, the effective damping of the system was measured by the logarithmic decrement technique, for a range of values of load resistance. The value of load resistance at which the effective damping doubles (compared to the open circuit case) is approximately equal to the output impedance of the piezoelectric sheets, neglecting structural damping in the beam. Figure 7 shows the measured

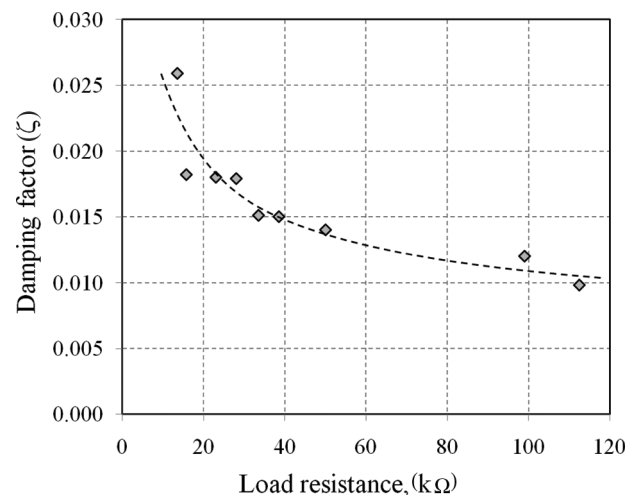


Figure 7. Variation of damping ratio with load resistance (in the absence of wind).

damping ratios, from which the output impedance of the piezoelectric sheets was determined to be between 25 and 40 k Ω . This is a convenient method to experimentally estimate the output impedance of the piezoelectric sheets, and therefore, the load resistance at which maximum power generation is expected.

Based on the damping ratio measurements, a range of load resistances from 5 to 300 k Ω was chosen for the power measurements. The transient voltage generated by the device was recorded with these load resistances at different values of incident wind velocity. Figure 8 shows the transient voltage measured at a wind velocity of 10 mph and a load resistance of 37 k Ω . The initial perturbations are seen to grow in amplitude till a steady state is reached. Note that the mean voltage at steady state is slightly negative. This can be attributed to errors arising from manual setting of the initial angle of attack. If the initial angle of attack is not exactly 0°, there will be a bias aerodynamic force acting on the tip body, which will result in galloping about a slightly deformed mean position. Also note that the amplitude of the steady-state response appears to contain an oscillatory component, which may be due to turbulence in the incident airstream. The maximum voltage generated is greater than 30 V (corresponding to an electric field of more than 157 kV/m), which is relatively high considering that the piezoelectric material constants (Table 2) are valid only in a linear region at small electric fields.

The output voltage predicted by the analysis at a wind velocity of 10 mph and a load resistance of 37 k Ω is shown in Figure 9. The trend of the predicted voltage closely approximates that of the measured voltage. Some discrepancy can be seen in the transient response; however, the steady-state behavior correlates very well with predictions. Note that the predicted voltage has a mean of zero and does not show any oscillatory variation of the steady-state amplitude.

It is interesting to explore the calculated angle of attack of the tip body and the tip displacement at this operating condition. The angle of attack (referenced to a line of symmetry of the tip body), shown in

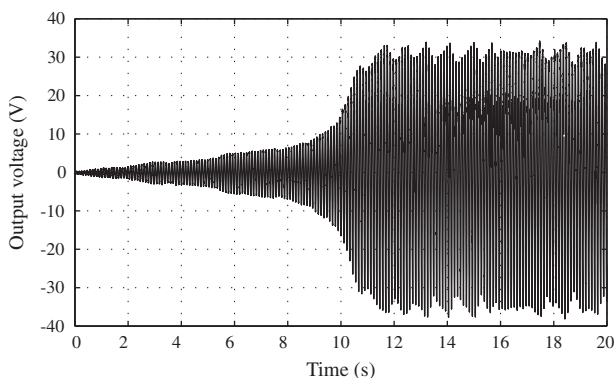


Figure 8. Measured output voltage, $V_\infty = 10$ mph, $R_l = 37$ k Ω .

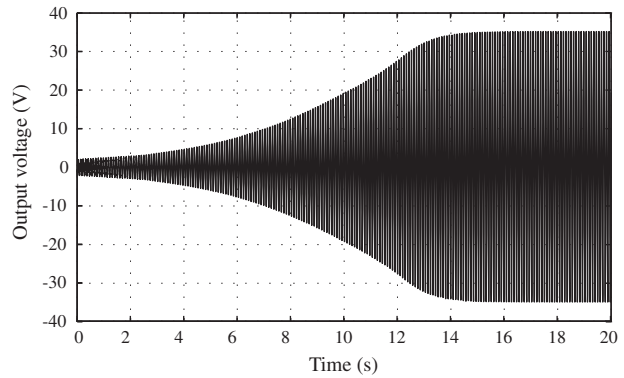


Figure 9. Predicted output voltage, $V_\infty = 10$ mph, $R_l = 37$ k Ω .

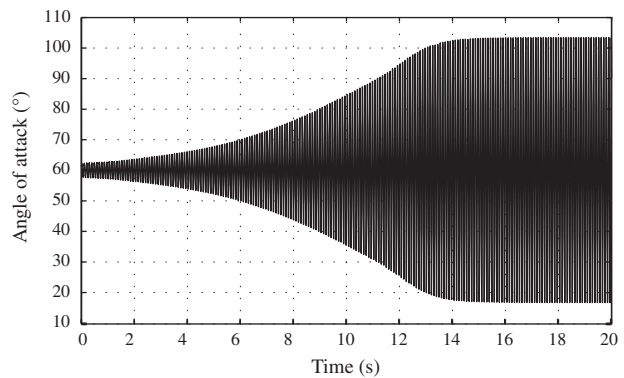


Figure 10. Predicted angle of attack of the tip body (referenced to a line of symmetry), $V_\infty = 10$ mph, $R_l = 37$ k Ω .

Figure 10, increases from around the mean of 60° till it reaches a steady state where it oscillates between a minimum of 16.7° and a maximum of 103.4°. A plot of the Den Hartog factor, $H(=dC_l/d\alpha + C_d)$, calculated from the measured sectional aerodynamic coefficients (see Figure 3) is shown in Figure 11. The small excursions around $\alpha = 40^\circ$ and $\alpha = 80^\circ$ could be due to experimental errors. It is seen that the Den Hartog factor is negative over a range of angles of attack approximately $25^\circ < \alpha < 95^\circ$, which is a smaller range than calculated for the present device (Figure 10). This indicates that the natural frequency of the present device is high enough that dynamic effects could be important. In addition, the analysis indicated that the peak-to-peak angle of attack variation at steady state increased with increasing incident wind velocity (Figure 12). Note that the peak-to-peak angle of attack variation corresponding to a negative Den Hartog factor is 70°.

The predicted tip displacement is shown in Figure 13. The maximum amplitude of the tip displacement is approximately 45 mm, which is considerable for a beam of length 167 mm. Durability of the device under such large fatigue loading could be a matter of concern and must be investigated in greater detail. In the case of the prototype device, several cracks developed across the

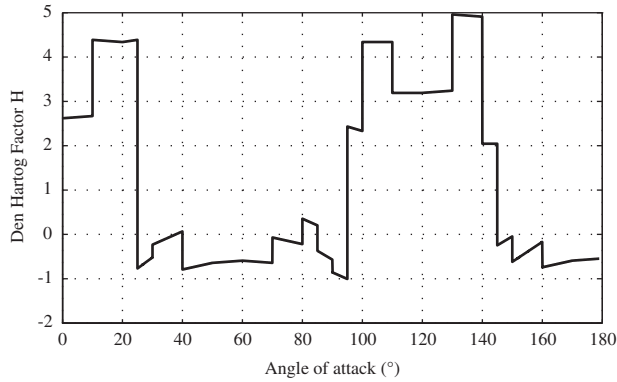


Figure 11. Den Hartog factor calculated from sectional aerodynamic coefficients measured by Alonso and Meseguer (2006).

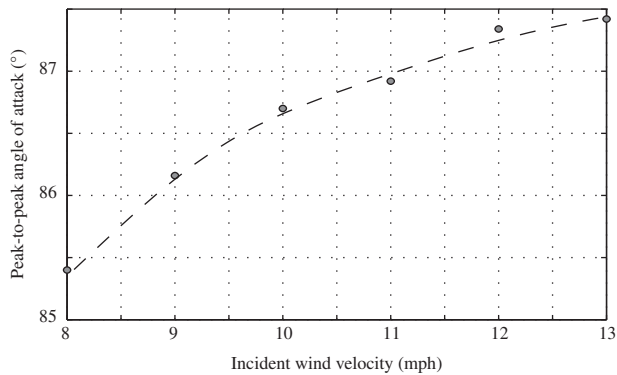


Figure 12. Predicted peak-to-peak angle of attack variation at steady state, $R_l = 37 \text{ k}\Omega$.

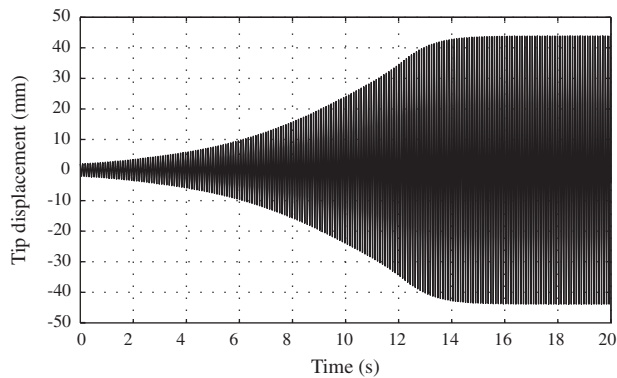


Figure 13. Predicted tip displacement, $V_\infty = 10 \text{ mph}$, $R_l = 37 \text{ k}\Omega$.

width of the piezoelectric sheets after a few experimental runs. Consequently, Young’s modulus of the piezoelectric material had to be reduced to approximately 50% in the analytical model to account for the loss in stiffness.

The measured output power (peak value) over the range of load resistances is shown in Figure 14. It is seen that the maximum output power is achieved at a

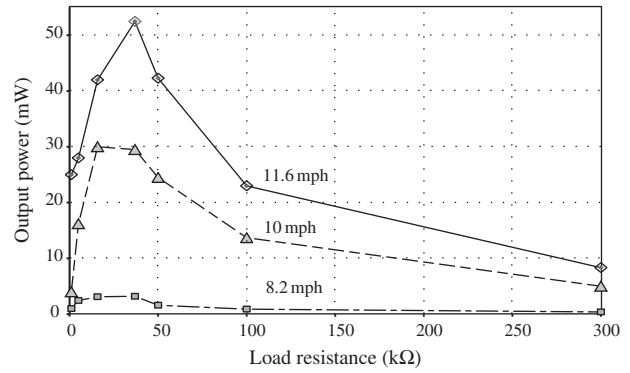


Figure 14. Variation of measured output power with load resistance.

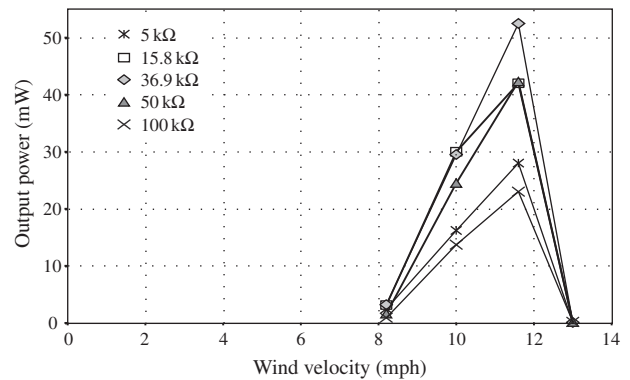


Figure 15. Variation of measured output power with incident wind velocity.

load resistance of approximately $37 \text{ k}\Omega$, which is close to the impedance of the piezoelectric sheets. As expected, the output power increases with increasing wind velocity. A maximum output power of 53 mW was measured, which is sufficient to power most of the wireless sensor nodes currently in use. This maximum power is significantly higher than that measured in a previous study of a galloping device (Sirohi and Mahadik, 2011) and is also much higher than achievable by means of vibrational energy harvesting.

The measured output power (peak value) over the range of wind velocities is shown in Figure 15. The device starts to extract power at wind speeds higher than approximately 8 mph . Therefore, this velocity can be considered as a cut-in velocity for extraction of power. However, the power abruptly drops to almost 0 for a wind velocity of 13.6 mph . This unexpected behavior is attributed to large-scale turbulence in the incident wind stream.

The correlation between experimental measurements and analytical predictions is shown in Figure 16 for an incident wind speed of 10 mph . The output power increases with increasing load resistance, reaches a maximum, and then decreases. The analysis is able to

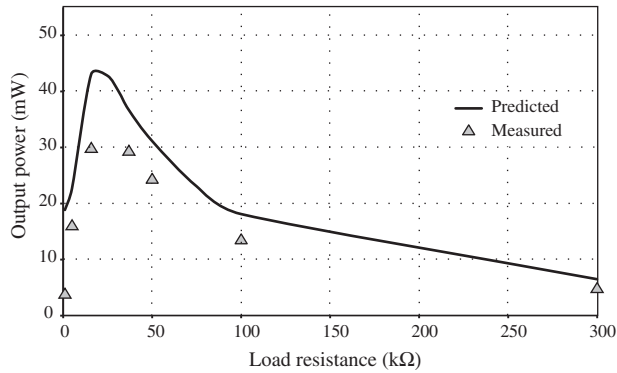


Figure 16. Correlation between measured and predicted output power for an incident wind speed of 10 mph.

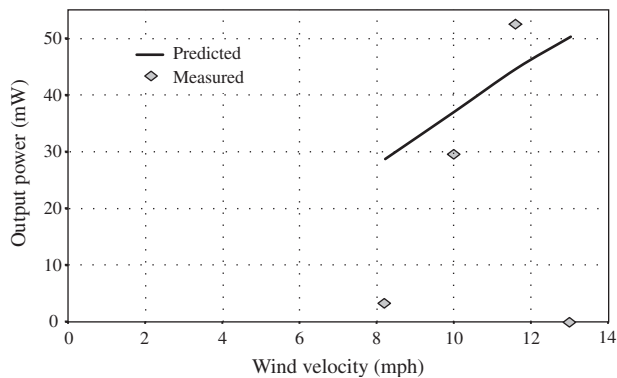


Figure 17. Correlation between measured and predicted output power for a load resistance of 36.9 kΩ.

capture the trend very well, but overpredicts the magnitude of the output power. This discrepancy can be attributed to several causes. First, the bond layer between the piezoelectric sheets and the beam is not modeled in the present analysis. The finite stiffness of the bond layer can cause a significant decrease in the energy transferred to the piezoelectric sheets. Second, the quasi-static aerodynamic analysis does not include any apparent mass effect of the air. This can be seen from the measured frequency of oscillations of the beam. In the absence of incident wind, the natural frequency of the beam was measured to be 10.43 Hz at a load resistance of 33.5 kΩ. The natural frequency varies by approximately 1.5% based on the value of load resistance (in the range 1–100 kΩ). The frequency of oscillations at a wind speed of 10 mph and a load resistance of 36.9 kΩ was measured to be 8.98 Hz. In comparison, the predicted frequency at 0 mph wind speed and at a wind speed of 10 mph is 10.6 and 10.55 Hz, respectively. The decrease in frequency in the presence of incident wind could indicate that apparent mass effects are significant and quasi-steady aerodynamics may not be sufficient to represent the behavior at these operating conditions. In a previous study of a galloping device

(Sirohi and Mahadik, 2011), the natural frequency of the device was lower and the predicted magnitude of output power was closer to the measurements. Finally, the piezoelectric material constants that were used in the analysis are valid only at small electric fields, assuming linear behavior. However, the piezoelectric material shows significant nonlinearities at higher electric fields such as those generated by the present device. For more accurate predictions, modified material constants will have to be used (Sirohi and Chopra, 2000).

The correlation between measured and predicted power over a range of incident wind velocities at a load resistance of 36.9 kΩ is shown in Figure 17. The analysis captures the trend and magnitude except for the drop in power at an incident wind velocity of 13.6 mph.

Conclusions and Future Work

A wind energy-harvesting device based on a galloping beam with piezoelectric sheets to convert mechanical energy into electrical energy has been fabricated, tested, and analyzed. The prototype device generated a maximum output power of more than 50 mW at a wind speed of 11.6 mph. This power level is sufficient to supply most of the commercially available wireless sensors currently in use and is significantly higher than that achievable from vibrational energy harvesting. The main advantages of this device are its simplicity and robustness. In addition, the mechanism of energy harvesting from galloping is inherently self-limiting. Therefore, no additional safety features need to be implemented to limit the motion of the device under high winds.

A coupled electromechanical model of the system was developed using quasi-steady aerodynamics. The model showed good agreement with the experimental data over a range of operating conditions. There were some discrepancies between the measurements and predictions, especially in terms of the natural frequency and magnitude of power output. It was concluded that at the natural frequency of the present system, approximately 10 Hz, apparent mass effects of the air could be significant. In addition, an abrupt decrease in output power at incident wind velocities greater than 13.6 mph were observed. This was attributed to large-scale turbulence in the wind tunnel and requires further investigation.

The galloping piezoelectric energy-harvesting device has been shown to be a viable alternative for powering wireless sensor nodes. Future work will involve investigation of the fatigue properties of the device, response to transient wind gusts, and refinements to the aerodynamic model.

Acknowledgments

The authors would like to thank the Cockrell School of Engineering for providing funding for this research and Dr. Ashish Purekar for his constructive suggestions.

References

- Ajitsaria J., Choe SY, Shen D and Kim DJ (2007) Modeling and analysis of a bimorph piezoelectric cantilever beam for voltage generation. *Smart Materials and Structures* 16: 447–454.
- Alonso G and Meseguer J (2006) A parametric study of galloping of two-dimensional triangular cross-section bodies. *Journal of Wind Engineering and Industrial Aerodynamics* 94: 241–253.
- Alonso G, Meseguer J and Prez-Grande I (2005) Galloping instabilities of two-dimensional triangular cross-section bodies. *Experiments in Fluids* 38: 789–795.
- Alonso G, Meseguer J and Pérez-Grande I (2007) Galloping stability of triangular cross-sectional bodies: A systematic approach. *Journal of Wind Engineering and Industrial Aerodynamics* 95(9–11): 928–940.
- Alonso G, Meseguer J, Sanz-Andres A and Valero E (2010) On the galloping instability of two-dimensional bodies having elliptical cross-sections. *Journal of Wind Engineering and Industrial Aerodynamics* 98: 438–448.
- Badrinath BR, Srivastava M, Mills K, Scholtz J and Sollins K (eds.) (2000) Special issue on smart spaces and environments. Guest Editorial, *IEEE Personal Communications*, Vol. 7, No. 5, Oct 2000, pp. 3.
- Barrero-Gil A, Alonso G and Sanz-Andres A (2010) Energy harvesting from transverse galloping. *Journal of Sound and Vibration* 329(14): 2873–2883.
- Blevins RD (2001) *Flow-Induced Vibrations*, 2nd edn. Malabar: Krieger.
- Bryant M and Garcia E (2011) Modeling and testing of a novel aeroelastic flutter energy harvester. *Journal of Vibration and Acoustics* 133: 011010-1–011010-11.
- Crandall SH, Karnopp DC, Kurtz EF Jr and Pridmore-Brown DC (1982) *Dynamics of Mechanical and Electromechanical Systems*. Krieger Publishing Company, Malabar, Florida.
- Den Hartog JP (1956) *Mechanical Vibrations*. New York: Dover Publications.
- Dietl J and Garcia E (2010) Beam shape optimization for power harvesting. *Journal of Intelligent Material Systems and Structures* 21(6): 633–646.
- duToit NE, Wardle BL and Kim S-G (2005) Design considerations for MEMS-scale piezoelectric mechanical vibration energy harvesters. *Integrated Ferroelectrics* 71:121–160.
- Elvin NG, Elvin AA and Spector M (2001) A self-powered mechanical strain energy sensor. *Smart Materials and Structures* 10: 293–299.
- Erturk A and Inman DJ (2009) An experimentally validated bimorph cantilever model for piezoelectric energy harvesting from base excitations. *Smart Materials and Structures* 18: 025009.
- Estrin D, Govindan R and Heidemann J (eds.) (2000) Special issue on embedding the Internet. *Communications of the ACM*, Vol. 43, No. 5, May 2000, pp. 38–41.
- Evans R and Bergman J (2007) Relationships between cropping sequences and irrigation frequency under self propelled irrigation systems in the Northern Great Plains (NGP). USDA Annual Report, Project Number: 5436-13210-003-02.
- Hagood N, Chung W and Von Flotow A (1990) Modelling of piezoelectric actuator dynamics for active structural control. *Journal of Intelligent Material Systems and Structures* 1(3): 327–354.
- IEEE. 1987. IEEE Standard on Piezoelectricity, ANSI/IEEE, Std. 176.
- Kauffman JL and Lesieutre GA (2009) A low-order model for the design of piezoelectric energy harvesting devices. *Journal of Intelligent Material Systems and Structures* 20: 495–504.
- Kazakevich MI and Vasilenko AG (1996) Closed analytical solution for galloping aeroelastic self-oscillations. *Journal of Wind Engineering and Industrial Aerodynamics* 65: 353–360.
- Kim S, Pakzad S, Culler D, Demmel J, Fenves G, Glaser S, et al. (2007) Health monitoring of civil infrastructures using wireless sensor networks. *Proceedings of the 6th International Conference on Information Processing in Sensor Networks*, April 25–27, Cambridge, MA, 254–263.
- Laneville A, Gartshore IS and Parkinson GV (1977) An explanation of some effects of turbulence on bluff bodies. *Proceedings of the Fourth International Conference on Wind Effects on Buildings and Structures*, Cambridge University Press, 333–341.
- Mainwaring A, Polastre J, Szewczyk R, Culler D and Anderson J (2002) Wireless sensor networks for habitat monitoring. *Proceedings of the 1st ACM International Workshop on Wireless Sensor Networks and Applications*, Atlanta, GA, 88–97.
- Mason WP (1950) *Piezoelectric Crystals and Their Application to Ultrasonics*. D. Van Nostrand Company, New York.
- Ottman GK, Hofmann HF and Lesieutre GA (2003) Optimized piezoelectric energy harvesting circuit using step-down converter in discontinuous conduction mode. *IEEE Transactions on Power Electronics* 18(2): 696–703.
- Ratkowski J (1961). Experiments with galloping spans. Paper 62, AIEE Winter General Meeting, New York.
- Robbins WP, Morris D, Marusic I and Novak TO (2006) Wind-generated electrical energy using flexible piezoelectric materials, IMECE2006-14050. *ASME Publications-AD* 71: 581–590.
- Roundy S, Wright PK and Rabaey JM (2004) *Energy Scavenging for Wireless Sensor Networks with Special Focus on Vibrations*. Kluwer Academic Publishers, Norwell, MA.
- Sirohi J and Chopra I (2000) Fundamental behavior of piezoceramic sheet actuators. *Journal of Intelligent Material Systems and Structures* 11(1): 47–61.
- Sirohi J and Mahadik RR (2011) Harvesting wind energy using a galloping piezoelectric beam. *Journal of Vibration and Acoustics* (accepted for publication).
- Sodano HA, Park G and Inman DJ (2004) Estimation of electric charge output for piezoelectric energy harvesting. *Strain* 40(2): 49–58.
- Tan YK and Panda SK (2007) A novel piezoelectric based wind energy harvester for low-power autonomous wind speed sensor. *Proceedings of the 33th Annual IEEE Conference of Industrial Electronics Society (IECON07)*, Taipei, Taiwan.
- Umeda M, Nakamura K and Ueha S (1996) Analysis of the transformation of mechanical impact energy to electric energy using piezoelectric vibrator. *Japanese Journal of Applied Physics* 35: 3267–3273.
- Wang DA and Ko HH (2010) Piezoelectric energy harvesting from flow-induced vibration. *Journal of Micromechanics and Microengineering* 20(2): 025019.

Wang N, Zhang N and Wang M (2006) Wireless sensors in agriculture and food industry recent development and future perspective. *Computers and Electronics in Agriculture* 50: 1–14.

Wang Y, Loh KJ, Lynch JP, Fraser M, Law K and Elgamal A (2006). Vibration monitoring of the Voigt bridge using

wired and wireless monitoring systems. *Proceedings of the 4th China–Japan–US Symposium on Structural Control and Monitoring*, October 16–17.

Yick J, Mukherjee B and Ghosal D (2008) Wireless sensor network survey. *Computer Networks* 52: 2292–2330.